ChemSusChem

Chemistry–Sustainability–Energy–Materials

Chemistry Europe

European Chemical Societies Publishing

Accepted Article

Title: A facile method to transform pickled olive wastes into sulfur-doped carbon for sodium-ion battery electrode

Authors: Alejandro Medina, Ricardo Alcántara, Pedro Lavela, and José L. Tirado

To be cited as: *ChemSusChem* **2024**, e202400708

Link to VoR: https://doi.org/10.1002/cssc.202400708

WILEY VCH

WILEY VCH

RESEARCH ARTICLE

A facile method to transform pickled olive wastes into sulfur-doped carbon for sodium-ion battery electrode

Alejandro Medina, Prof. Ricardo Alcántara*, Prof. Pedro Lavela, and Prof. José L. Tirado

A. Medina, Prof. R. Alcántara, Prof. P. Lavela, Prof. J.L. Tirado
IQUEMA. Department of Inorganic Chemistry
University of Cordoba
Campus Universitario de Rabanales. Edificio C3, primera planta. 14071 Córdoba (Spain)
* E-mail: ralcantara@uco.es

Abstract: This work provides a novel, low-cost, and effective method to prepare disordered carbon materials for advanced sodium-ion batteries using biomass. A large amount of olive stone waste is yearly produced in the world, and it could be re-used for fine applications other than fuel for heat production. After treatment with sulfuric acid solution and carbonization process, wastes of olive stone are efficiently transformed into optimized carbon electrode material. XRD, XRF and XPS, electron microscopy, and physical gas adsorption are used for the compositional, microstructural, and textural characterization of the carbons. During the synthesis, impurities are removed, C-S links are formed and micropores pores are created. Sulfuric acid acts like S-dopant. The latent pores, or pores closed to nitrogen, can be found using CO_2 adsorption, and are very suitable for accommodation for sodium. The results reveal that the reversible capacity is raised from ca. 200 mAh g^{-1} to ca. 250 mAh g^{-1} for the carbon obtained through treatment with sulfuric acid. The improved electrochemistry is the result of the s-doping and the porosity.

Introduction

Since sodium is abundant and low-cost compared to lithium, sodium-ion batteries (SIBs) are more sustainable than lithium-ion batteries. The most common anode material in SIB is a non-graphitic carbon [1]. Although hard-carbon anode materials are often obtained using glucose as a precursor, the laws of the EU prevent using substances that can be employed as foods for other types of industrial purposes. In contrast to that, using agricultural wastes as materials for SIBs can be particularly useful. Around 8 million tons of olives are typically produced each year in Spain including table and oil olives, and a total of 23.6 million tons were worldwide production in 2020. Between 10 and 20% corresponds to the stone in the total mass of the olives. In a circular economy, it is very interesting to transform trash into treasure, and biomass-derived carbon can be very useful for energy storage systems, such as batteries and supercapacitors [2].

A typical precursor to obtain carbon is the pyrolysis of organic matter, although the high temperatures usually employed (typically 1200-1400 °C) are inconvenient [3]. An alternative method to produce carbon from biowaste could be hydrothermal carbonization [4]. However, the hydrothermal method is not easily scaled up.

Since olive stone is an abundant agricultural waste, particularly in the Mediterranean region, we have used a new method to obtain carbon from olive stone which can be employed as a negative electrode in SIB. This method is low-temperature (800 °C) and easily scaled-up. The olive stones have been treated with sulfuric acid (AC) before the thermal treatment and compared with the olive stones non-treated with acid (NAC). Sulfuric acid is a low-cost and inorganic chemical produced in the largest quantity worldwide, and it can be easily recovered and recycled [5].

The mechanism of intercalation of sodium into disordered carbons is the subject of previous studies [1, 6]. For example, it was concluded that the microstructure, surface area, and porosity must be tailored to increase the capacity of the carbon in the battery and to decrease the irreversible trapping of sodium ions. Thus, latent pores can contribute very efficiently to the reversible storage of sodium in the form of clusters [8]. Doping of carbonaceous materials with heteroatoms such as sulfur can be an efficient method to optimize the properties of these electrode materials for sodium-ion batteries [9a,b], as well as doping with other heteroatoms for other ion batteries [9c,d]. Tailoring the porosity and controlling composition and microstructure often involve sophisticated methods. We propose here a novel strategy to obtain optimized carbons through the transformation of wastes of salted olive stones into S-doped carbon with tailored porosity. In addition, the mechanism of the intercalation of sodium into the carbonaceous samples prepared here is explored to see the effect of the treatment with sulfuric acid, for example calculating the diffusion coefficient of sodium and recording impedance spectra.

Results and Discussion

Conversion from waste to carbon

Carbon samples were obtained using the procedure schematically shown in Scheme 1. The pretreatment with a sulfuric acid solution of pickled green olives is used to remove impurities, initiate the dehydration process, activate the carbonization process, and improve the properties of the resulting carbon. Thus, the soluble salts and biominerals present in the biomass are dissolved in the acid solution. For the sake of comparison, a sample was also prepared using just distilled water instead of sulfuric acid. Simple washing with distilled water is not as efficient as the acid treatment with sulfuric acid solution. It is worth noting that the carbonization temperature employed in this synthesis (800 °C) is significantly lower than the temperatures employed in many cases for the preparation of carbon for SIB

(typically 1200 °C), and it reduces the economic cost and improves the sustainability of the procedure.

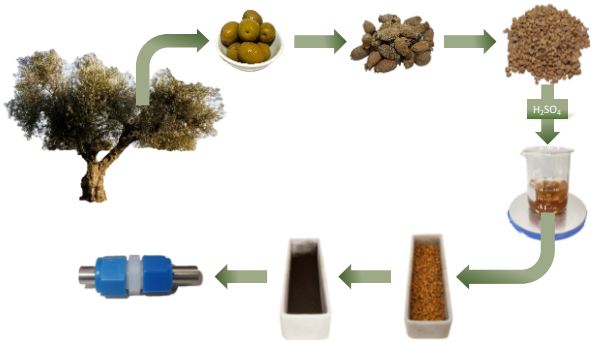

Scheme 1. Process of fabrication of carbon for batteries from cured olives.

Composition and element surface analysis

The chemical composition of the olive stones, including both volatile and non-volatile compounds and chemical elements, can influence the properties of the resulting carbon electrodes. The composition can be studied by TGA, XRF, EDS, and XPS. According to the weight loss displayed in Fig. 1, the content of non-volatile matter, or ashes, in NAC is 7.4%, while all mass was lost in AC, revealing its purity. In fact, the main element impurities (Na, Ca. Cl, K, and P) are almost absent in the XRF analysis of AC (Table 1), due to their solubility in the sulfuric acid solution. The results of the EDS microanalysis coupled with SEM also confirm that the carbon content is higher in AC. Since EDS microanalysis is a semiquantitative technique, the concentrations of the elements detected in the form of traces are given as lower than 1% in Table 1. All these results evidence the superior capacity of the acid treatment to leaching of elements that are not eliminated by washing with water and simple heating and hence promote a higher carbon yield. On the other hand, it is observed the presence of a small amount of sulfur (Table 1), and this fact will be examined below in the light of XPS. It is concluded that the acid treatment leaves behind sulfur atoms on the particle surface of AC.

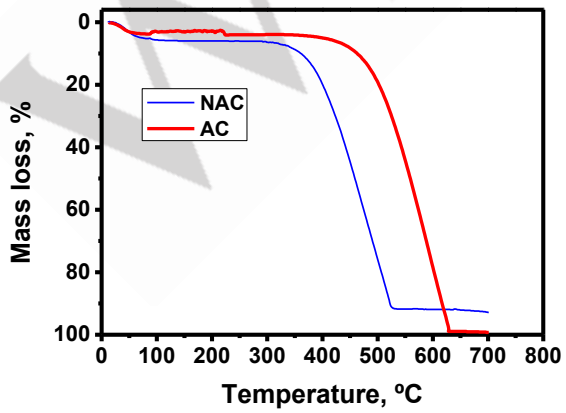

Figure 1. TGA curves of olive stone samples.

Table 1. Composition (wt. %) determined from XRF and EDS measurements.

	XRF NAC	XRF AC	EDS NAC	EDS AC
C	-	-	87.98	94.73
O	-	-	7.03	4.79
Na	3.27	0.34	1.3	<1
Cl	4.1	-	2.03	<1
Ca	1.49	0.27	1.03	<1
K	0.56	-	<1	<1
S	-	0.20	<1	<1
P	0.13	-	<1	<1

The composition of the surface can be determined by XPS analysis (Fig. 2). The XPS quantitative analysis of the elements is shown in Table 2. The surface of AC is cleaner, with more relative contribution of carbon and less oxygen. The observed binding energy in the sulfur 2p core level, with the two components S 2p1/2 at 165.4 eV and S 2p3/2 at 164 eV, clearly is not coming from any sulfate, but it is ascribed to sulfur bonded to carbon [9]. Sulfur is not detected on the surface of NAC by XPS. This sulfur (C-S) on the surface of AC is produced during the reaction between traces of sulfuric acid employed during the acid treatment and the carbonaceous sample during the annealing under an Ar flow. According to previous studies, the S-doping of carbon can improve sodium storage [9].

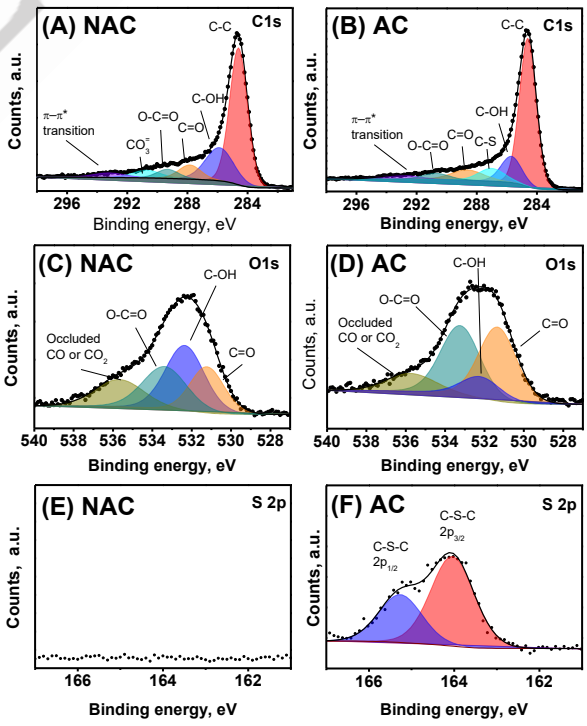

Figure 2. Detailed views of the XPS spectra at the C 1s (A, B), O 1s (C, D), and S 2p (E, F) core levels of NAC and AC samples.

The depth of the analysis can contribute to the differences observed between the different chemical composition results, depending on the analysis instrument. For example, in the XPS results (penetration depth of 10-100 Å) the analysis is indicative of a sulfur-rich surface, compared to the XRF (depth of several millimeters) and EDS (typically between 0.1 μm and 10 μm of depth).

In the spectra at the C1s core level, for NAC, six components were decomposed from the asymmetric profiles in which chemical shifts are assigned to graphitic carbon (284.6 eV), C-OH (285.87 eV), C=O (287.83 eV), carboxyl (289.31 eV) and carbonate (290.7 eV) groups (Fig. 2 a and b), and also, a broadened band, commonly attributed to shake-up satellite peaks due to π–π* transitions in aromatic rings is visible at ca. 292 eV [11]. For the fitting of AC, the carbonate disappears and the contribution from C-S emerges.

The sub-spectra at the O1s core levels are sensitive to changes in the functionality of oxygenated groups located at the surface, and the main difference is that the acid treatment reduces the relative contribution of C-OH (531.2 eV).

Table 2. Elemental surface analysis (atomic %) obtained from the XPS fitting.

	Group	NAC	AC
Na 1s		3.7	0.93
S 2p	C-S	-	1.38
C 1s	C-C	45.46	54.72
	C-OH	17.41	12.02
	C=O	5.9	7.5
	O-C=O	3.71	3.68
	CO_3^{2-}	4.01	-
	C-S	-	7.38
	π-π*	2.69	3.36
O 1s	C=O	3.88	3.49
	C-OH	6.64	1.06
	O-C=O	3.68	3.4
	CO/CO_2	2.9	1.08

Microstructure

The XRD results can be used to follow how the treatment with sulfuric acid regulates the crystalline impurities and the microstructure. The XRD pattern of NAC (Fig. 3Aa and Ba) contains broad reflections due to non-graphitic carbon and narrower reflections due to NaCl (halite) as the major impurity and $CaCO_3$ (calcite) as a minor impurity. After acid treatment, the reflections of NaCl are not observed (Fig. 3Ab and Bb). These results further corroborate the efficiency of the treatment with sulfuric acid to remove impurities. After looking at the detailed view of the XRD patterns in the region between 5 and ca. 30 °2θ (Fig. 3B), it is observed that the (002) reflection is less broadened and more intense for AC, indicating a more crystallization degree after acid treatment. The broad diffraction (100) at ca. 43 ° 2θ is also narrower for AC. On the other hand, the (002) reflection is slightly centered are lower angles for AC, in good agreement with a certain expansion of the interlayer spacing due to the S-doping, because the atomic radius of S is larger than C radius. Fitting the XRD patterns with Rietveld refinement, the resulting d_{002} values are 0.379 nm and 0.391 nm for NAC and AC, respectively.

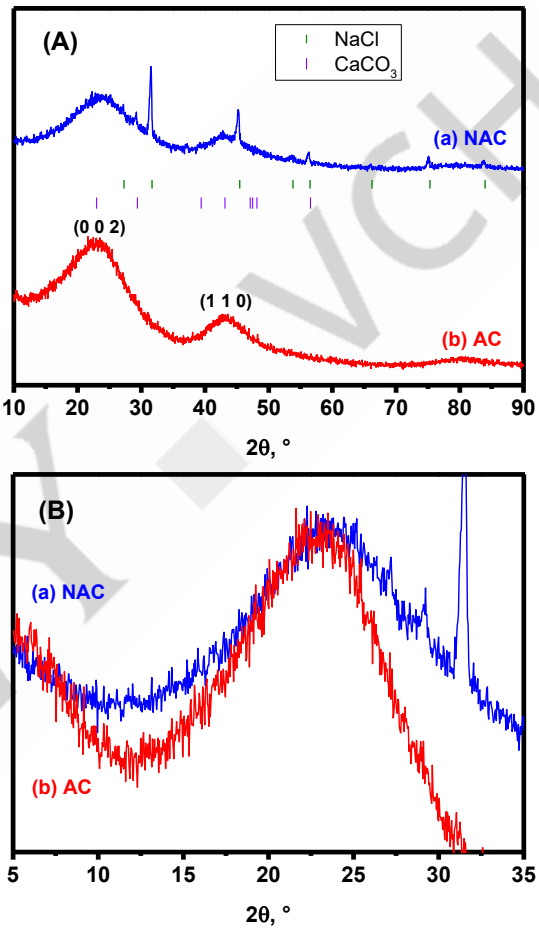

Figure 3. (A) XRD patterns and (B) a detailed view in the range between 5 and 35 °2θ.

In the SEM micrographs, it is observed that the sulfuric acid treatment changes the particle morphology. The micrometric particles of AC exhibit cavities of around ten microns in diameter, while the particle surface is flatter for NAC (Fig. 4). This result agrees well with the acid attacks the olive stone and eliminating matter that produces cavities or pores. This modification of microtexture can influence the electrode/electrolyte interface. Although, according to the EDS microanalysis, sulfur atoms are present in the samples in a tiny amount, it was worth recording a mapping of composition after a prolonged accumulation of scans. According to the selected mapping of composition, sulfur atoms are homogeneously distributed (Fig. 4e).

The TEM image of AC unveils closed and smaller pores in AC compared to NAC (Fig. 5a,b). Fringes of the crystalline impurities (NaCl and $CaCO_3$) and nanocrystalline domains are observed in the HRTEM images of NAC (Fig. 5c). In Fig. 5d, the observed

interlayer spacing is expanded in AC (d_{002} = 0.391 nm) compared to graphite (d_{002} = 0.335 nm). The fast-Fourier Transform (FFT) performed in the HRTEM images allows us to obtain a diffraction pattern with spots which is characteristic of a polycrystalline material for NAC, while spots are not observed in AC (Fig. 5d).

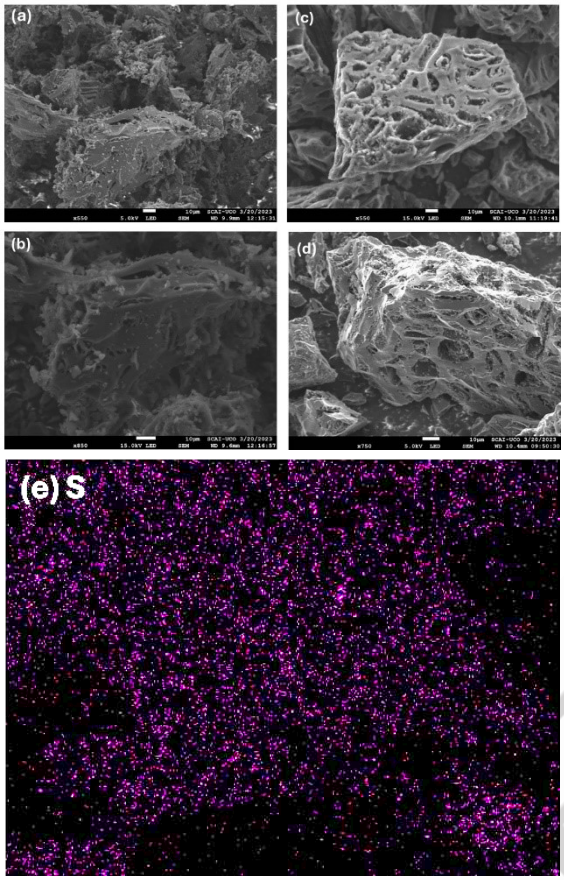

Figure 4. SEM micrographs for NAC (a and b) and AC (c and d), and (e) EDS mapping of S corresponding to image (c).

Raman spectra were recorded to further characterize the order/disorder of the carbonaceous samples. The Raman spectra of the carbon samples reveal two bands which are centered at ca. 1350 cm^{-1} and ca. 1600 cm^{-1}, respectively (Fig. 6). These spectra were fitted using five Gaussian peaks (D1, D2, D3, D4, and G), following the literature [12]. The intense peak labeled D1 is centered at 1349 cm^{-1} and is assigned to disordered domains and defects in the graphitic structure, and it is a vibration mode forbidden in perfect graphite. The intense peak labeled G is assigned to the in-plane displacement of carbon atoms in graphene sheets of graphitic (or pseudo-graphitic) nanodomains, which corresponds to the lattice vibration mode with E_{2g} symmetry in graphite. Additional n-order bands are also observed (D2, D3, and D4). Just a subtle difference is observed in the comparison of the two samples. The ratio between the heights of the main two peaks (I_{D1}/I_G) is slightly lower for AC (1.01) than NAC (1.15), and the calculated relative area of the G band is higher for AC (Table 3), indicating more crystalline nanodomains of graphite in AC, in good agreement with the XRD results. From the ratio of the areas of G and D1 peaks, the calculated crystallite sizes (L_a) are 1.9 nm and 2.2 nm for NAC and AC, respectively. Most probably, the chemical attack of sulfuric acid initiates the carbonization process before the thermal annealing.

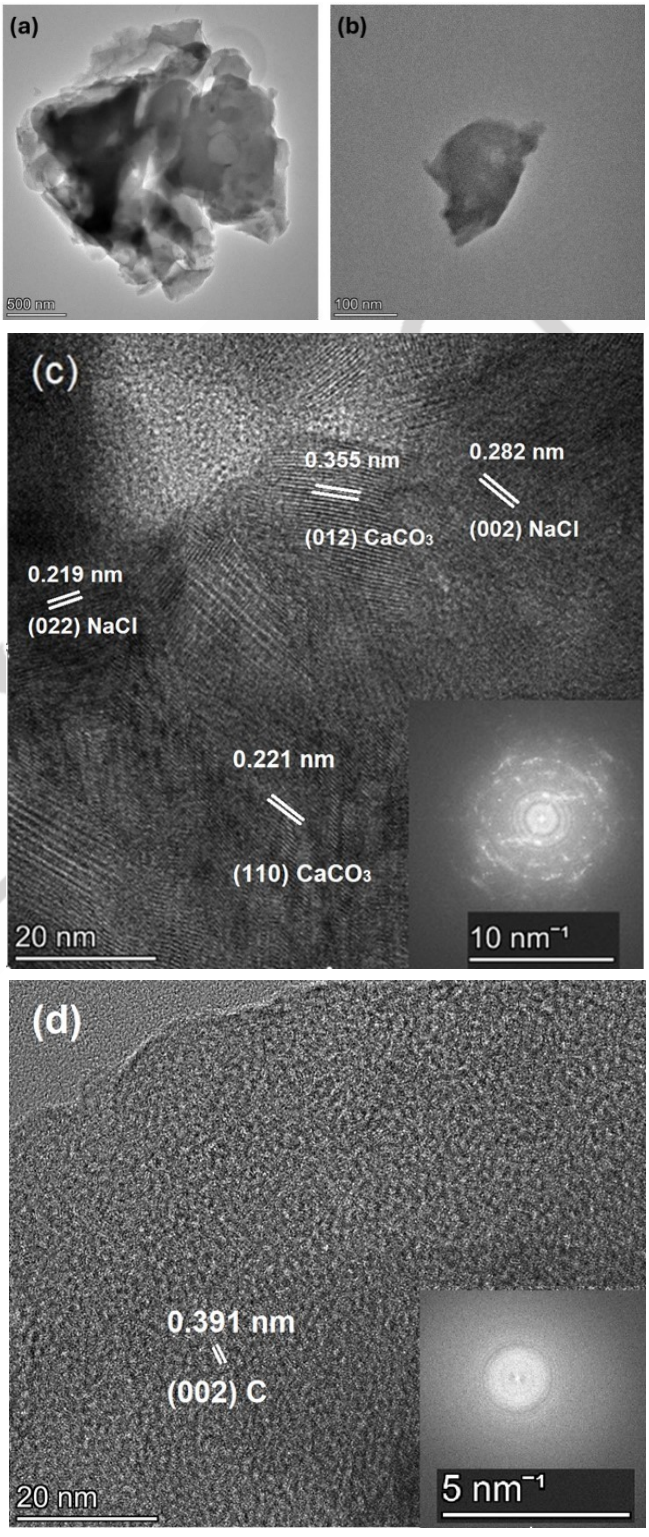

Figure 5. TEM micrographs of NAC (a) and AC (b). HRTEM micrographs of NAC (c) and AC (d). FFT images are shown as an inset in (c) and (d).

10.1002/cssc.202400708

RESEARCH ARTICLE

Table 3. Relative area (%) of the Gaussian bands in the Raman spectra.

	NAC	AC
G	14.35	19.59
D1	33.76	40.71
D2	13.6	9.94
D3	18.16	13.12
D4	20.12	16.63

As a conclusion, there are two opposite phenomena. Firstly, the sulfur atoms are rather located on the surface of the carbon particles, and it is expected that create point defects on the surface. On the other hand, the sulfuric acid treatment (involving dehydration of organic molecules and dissolution of inorganic salts) accelerates the graphitization process, irrespective of the point defects on the particle surface.

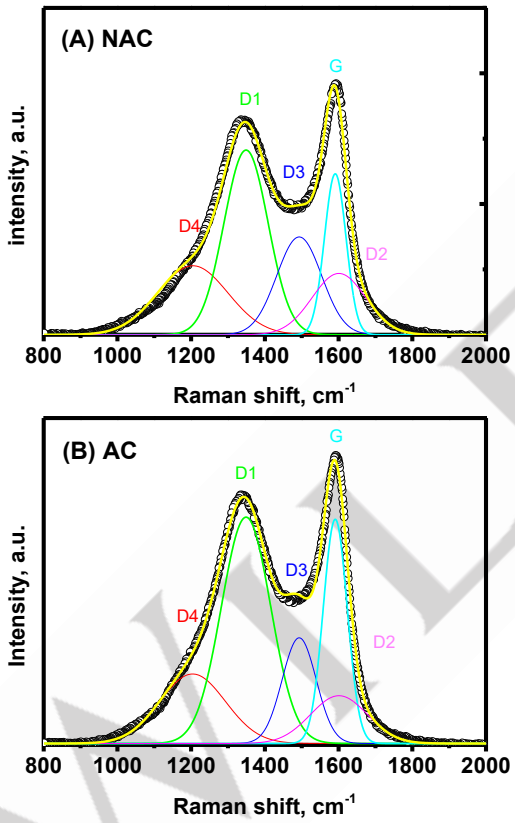

Figure 6. Raman spectra of NAC and AC and fitting of them.

Textural properties

Gas physisorption was conducted to investigate the surface area and porosity of the carbon samples. The porosity in these samples is not simple, and then we have employed a strategy based on the comparison of different adsorbates and the use of different types of calculations. It is known that carbon dioxide adsorption can be an alternative to nitrogen for the characterization of micropores and ultramicropores [13a,b]. Thus, nitrogen (77 K) and carbon dioxide (273 K) were employed as adsorbates. The thermal decomposition of the organic precursors and the evolved gases can create pores, and the minerals dissolved with acid can leave behind cavities. The rapid nitrogen adsorption observed for NAC (Fig. 7) at low pressures demonstrates the presence of micropores accessible to N_2. Complicated pores can lead to difficulties in nitrogen desorption and other techniques are needed to study closed pores [13]. The carbons with very narrow pores (micropores and ultramicropores) and tortuosity can exhibit large hysteresis in the isotherms, and nitrogen adsorption is not adequate for studying their microporosity. The nitrogen isotherms have anomalous behavior, particularly in the desorption branch, and this procedure is not adequate to calculate the pore size. The hysteresis in the nitrogen isotherm of NAC is also indicative of mesoporosity. These two samples are microporous (< 2 nm), and a larger micropore area and volume are obtained for NAC from the t-plot (Table 4). The pores that are too small to the adsorbate gas cannot be recognized as pores by the adsorbate, or in other words, are nitrogen-closed pores or latent pores. This is irrespective of pores that could be even closed for CO_2 adsorption.

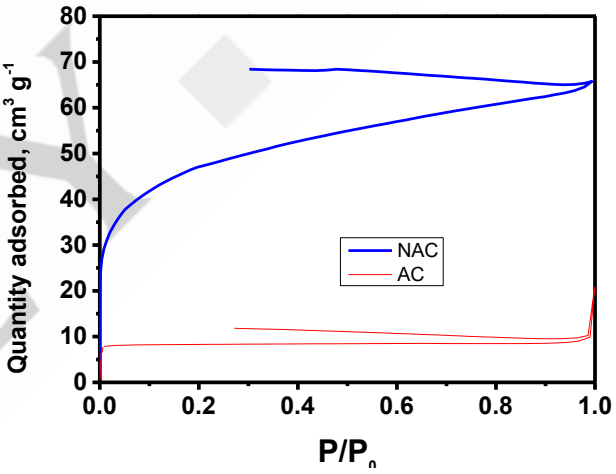

Figure 7. Adsorption-desorption isotherms for N_2 (77 K).

Adsorption of CO_2 can be an alternative to nitrogen (Fig. 8), more suitable for measuring the microporosity in these samples, mainly because CO_2 diffusion at 273 K is more rapid [13a,b, 14]. Dubini-Radushkevic (DR) method was employed to calculate the surface area and micropore volume with CO_2 adsorption. It is found that both AC and NAC possess large surface areas due to micropores and ultramicropores (< 0.7 nm). The surface area of AC measured with carbon dioxide is larger than NAC, due to the micropores and ultramicropores (Table 4), in contrast to the results with nitrogen adsorption. The diffusion of nitrogen in the micropores of AC is very slow and these pores are accessible by CO_2 but not by N_2. The latent pores can contribute to increasing the capacity for electrochemical accommodation of sodium ions, while the molecules of the solvent with larger size cannot diffuse into the small pores, particularly the “extra” ultramicropores of AC which are not accessible to nitrogen.

Table 4. Surface and porosity properties.

	CO_2 NAC	CO_2 AC	N_2 NAC	N_2 AC
S_{BET}, $m^2\ g^{-1}$	-	-	168.3	37.2
t-plot external area, $m^2\ g^{-1}$	-	-	42.9	0.83
t-plot micropore vol., $cm^3\ g^{-1}$	-	-	0.057	0.013
t-plot micropore area, $cm^2\ g^{-1}$	-	-	125.4	35.5
Langmuir area, $m^2\ g^{-1}$	-	-	204.2	36.3
DFT- total pore area $m^2\ g^{-1}$	-	-	60.0	5.5
DR equiv. surface, $m^2\ g^{-1}$	505.5	536.7	-	-
DR micropore vol., $cm^3\ g^{-1}$	0.203	0.249	-	-

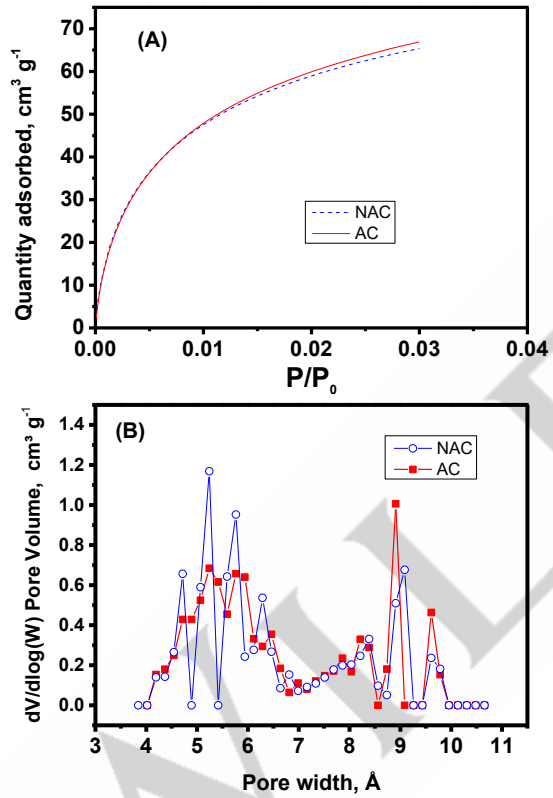

Figure 8. (A) Adsorption isotherms for CO_2 (273 K) and (B) the corresponding pore size distribution.

Galvanostatic cycling

In Fig. 9 A and B, the voltage curves are displayed. In the first discharge, three regions can be distinguished, the irreversible pseudoplateau near 0.8 V, the sloped region, and the pseudoplateau below 0.2 V. In the region near ca. 0.8 V, the SEI is irreversibly formed during the first discharge, and it contributes to the irreversible consumption of sodium during the first discharge. The capacity of the region between ca. 0.2 and ca. 1.0 V in the charge is particularly more extended for AC. The formation of defects in the graphene layers related to C-S links and the larger distance between the graphene layers can increase the capacity of the sloped region for AC. Thus, Bommier et al. found through DFT calculations that the defects of the graphene layers increase the "ionic storage" in the sloped region [6b]. In the discharge curve, the low-voltage pseudoplateau in the region below ca. 0.2 V, which is associated with the filling of latent pores with sodium, the capacity of AC (ca. 100 mAh g^{-1}) is significantly larger than NAC (ca. 50 mAh g^{-1}), due to the porosity.

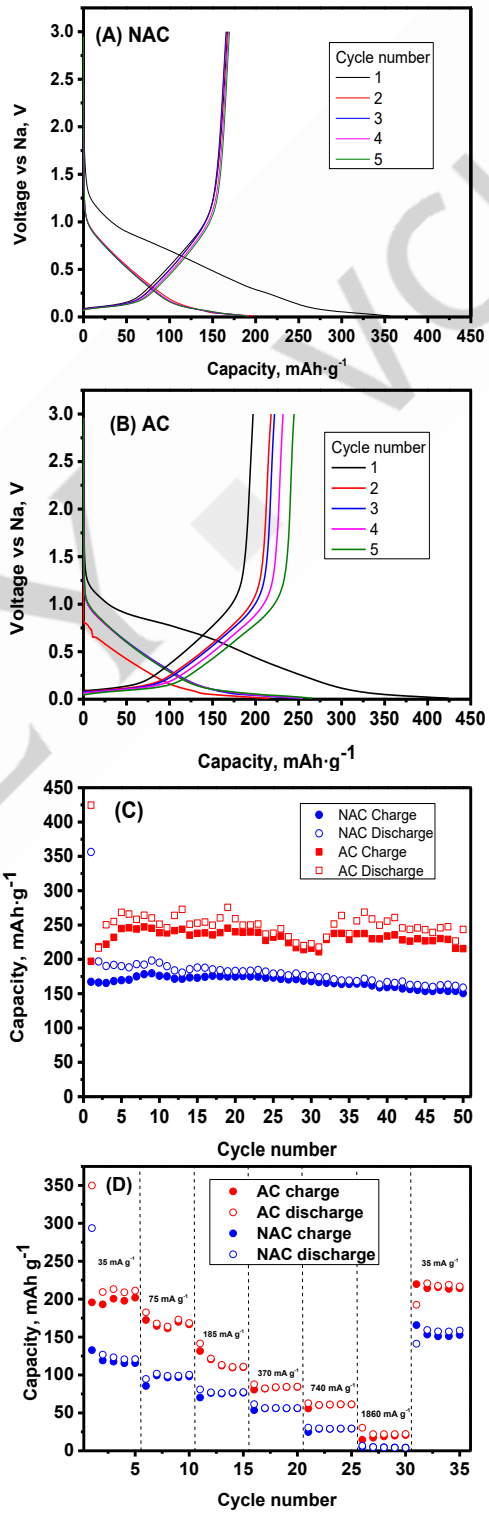

Figure 9. Electrochemical results of NAC and AC in sodium-half cells. Voltage-capacity curves for NAC (A) and AC (B). (C) Capacity as a function of cycle number. (D) Rate performance.

The total reversible capacity is increased from ca. 200 mAh g^{-1} to ca. 250 mAh g^{-1} after acid treatment (Fig.9C). In good agreement with other studies, these results confirm that the latent pores in AC are very suitable for storing sodium clusters [6d]. On the other hand, the reversible capacity slightly increases during the first few cycles for AC, indicating an activation process, which may be related to changes (e.g. swelling) in the pores. In the cycling experiments carried out at variable kinetics (Fig. 9D), AC also exhibits better rate performance. At 185 mA g^{-1} of current intensity, the capacity of AC is 110 mAh g^{-1}.

Cyclic voltammetry, GITT, and diffusion coefficient

In the CV (Fig. 10a) at a slow rate (1 mV s^{-1}), a broad reduction peak is observed which is centered at ca. 0.4 V, and it is ascribed to ionic insertion. The reductive current below ca. 0.3 V is due to the formation of clusters of metallic sodium. At a higher rate (10 mV s^{-1}) the reductive peak is less defined (Fig. 10b). The maximum mass-normalized intensities observed in the oxidative and reductive peaks in the CV are delivered by AC at the two scan rates, suggesting an easier and more rapid reaction.

From GITT experiments, the voltage curves under quasi-equilibrium conditions can be measured. After the first galvanostatic discharge-charge cycle for activation and formation of the SEI, the GITT curves of the second discharge are plotted in Fig. 11A. The voltage of the AC sample falls more rapidly and arrives easily at the region below 0.2 V, indicating that the mechanism for sodium storage is different. This result can be interpreted in terms of a mechanism more based on the formation of metallic sodium clusters for AC, and a mechanism more like sodium-ion adsorption on graphene layers in the no-acid sample. Sodium clusters are more easily formed in AC.

The relaxation curves obtained in the GITT experiments were employed to calculate the diffusion coefficient as was previously described elsewhere [2c]. The diffusion coefficient of sodium is one order of magnitude higher in AC than in NAC (Fig. 11B). This result agrees well with the higher capacity values and is consistent with a modification of the microstructure of the carbon. Thus, it is confirmed that the effect of the acid treatment is not just a simple removal of impurities, and the formation of defects in the graphene layers of AC, the expansion of the interlayer spacing, and the S-doping can contribute to this optimized electrochemical behavior. The expansion of the interlayer spacing due to S-doping, and the formation of S-related defects and sodium clusters in the latent pores below ca. 0.2 V can contribute to a decrease in the diffusion coefficient. Chen et al. reported that the formation of C-S bonds can decrease the energy barrier for sodium diffusion [9a].

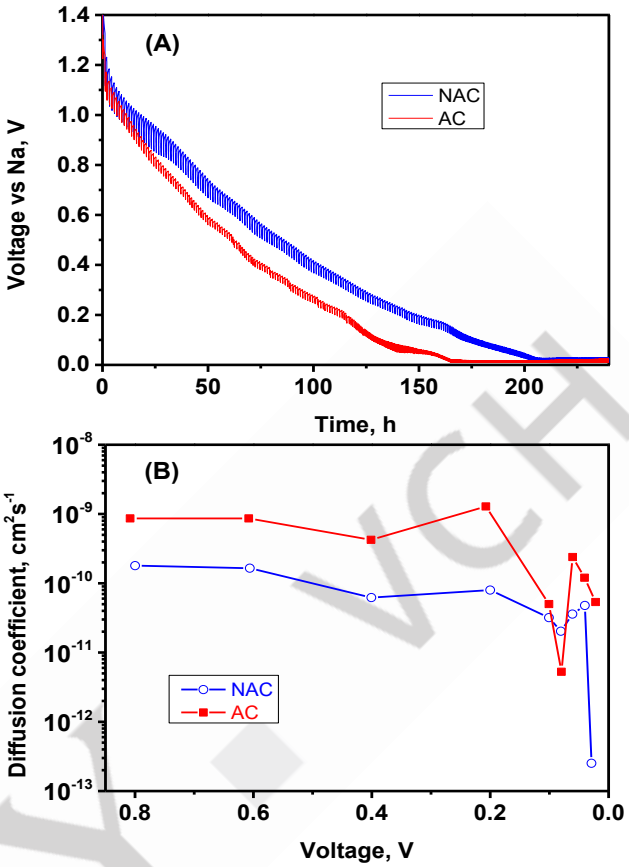

Figure 10. CV of sodium half-cells at two different scan rates, in the voltage range between 0.0 and 3.0 V.

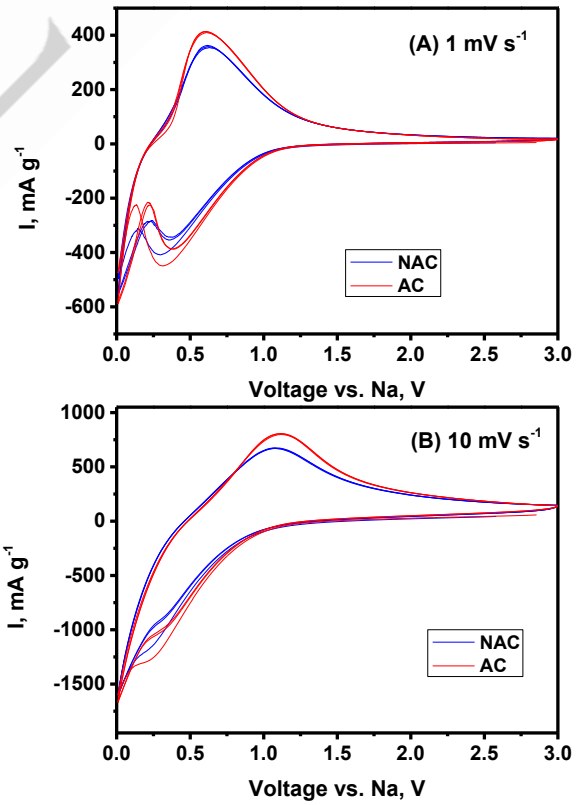

Figure 11. (A) GITT curves and (B) Calculated diffusion coefficient values for sodium ions in carbon electrodes.

Impedance spectra

A better understanding of the interfacial properties can be achieved by electrochemical impedance spectroscopy (EIS) experiments. In the Nyquist plots (Fig. 12), the sizes of the semicircles of AC are larger for both the fresh (uncycled) cell and after five cycles, indicating better interfaces for AC. The two typical semicircles are better observed for AC after the fifth discharge. The semicircle at the high-frequency region is due to sodium migration through the SEI, while the semicircle at medium frequencies is due to the charge transfer [14]. After fitting with the equivalent circuit, it results that the resistance of the SEI (R_2) is smaller for AC (Table 5). The pores and the sulfur atoms could contribute to improving the contact between the AC electrode and the electrolyte and more rapid sodium diffusion through the passivating layer.

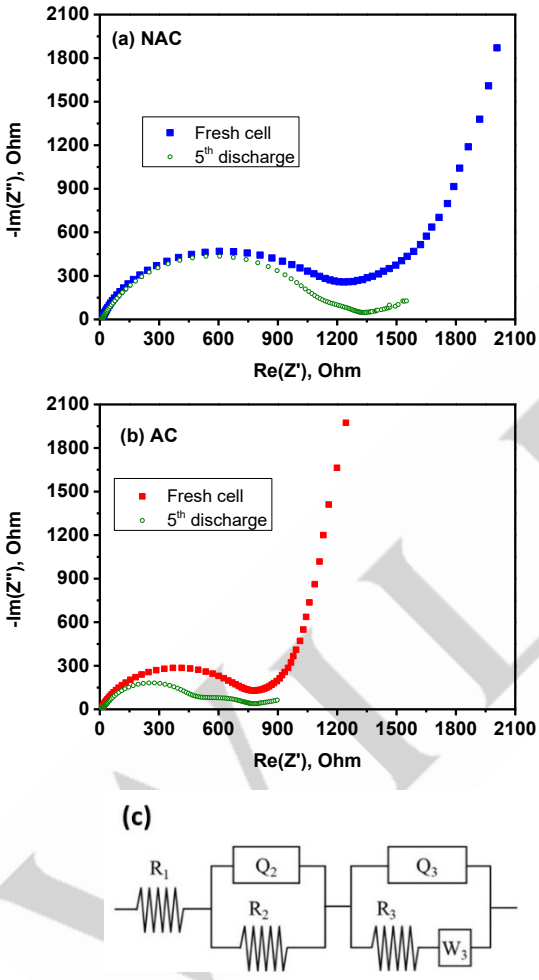

Figure 12. Nyquist plots of NAC (a) and AC (b) in sodium cells, and (c) the proposed equivalent circuit.

Table 5. Results of the fitting of the EIS after the fifth discharge with the equivalent circuit.

	NAC	AC
R_1, Ohm	9.8	7.9
R_2, Ohm	1085	414.3
Q_2, F s^{-a}	4.2 10^{-6}	8.4 10^{-6}
a_2	0.82	0.78
R_3, Ohm	361.6	379.5
s_3, Ohm $s^{-1/2}$	10.10	6.26
Q_3, F s^{-a}	2.08 10^{-3}	1.03 10^{-3}
a_3	0.39	0.41

Conclusion

The present work describes a facile and low-cost method to obtain carbon from olive stone wastes which can be efficiently employed in sodium-ion batteries. Thus, this is a sustainable way to transform trash into treasure. The treatment with sulfuric acid not only removes impurities and increases the carbon yield, but also induces the formation of C-S bonds, modifies the texture, and improves the electrochemistry. The heteroatoms (sulfur) and the latent pores (inaccessible to N_2 adsorption but accessible to CO_2) contribute to more active sites for reversible sodium capture and expand the distance between the carbon sheets. The carbon that is obtained with this method delivers a higher reversible capacity of ca. 250 mAh g^{-1}, and its impedance and diffusion of sodium are improved. These findings promote the circular economy and can make the SIBs even more competitive.

Experimental Section

Materials preparation

Olive stones obtained from the waste of table olives were used as the starting material for obtaining non-graphitic carbon samples. The olives were purchased from a market, and then the olive stones were obtained and used as carbon precursors. For that, the commercial olive stones were washed with distilled water and ground with a hammer. In the first procedure, carbon was obtained by annealing the stones in a furnace under an Ar-flow at 800 °C for 1 h, and then ground, and this sample is referred to as “no acid carbon (NAC)”. Alternatively, the stones were treated with a solution of 10% sulfuric acid (Panreac) solution before the annealing step, and then washed with distilled water, and this sample is referred to as “acid carbon (AC)”.

Materials characterization

Thermogravimetric analysis (TGA) was performed in an air atmosphere and using a Shimadzu instrument. To determine the chemical compositions of the samples, a Rigaku Primus IV X-ray fluorescence (XRF) spectrometer, and an SEM microscope equipped with a probe with energy dispersive X-ray spectrometer (EDS) microanalysis were used. To study the surface chemistry of carbon particles, XPS was employed, with a SPECS Phobios 150 MCD spectrometer using monochromatic Al Kα radiation (1486.71 eV), and the spectra were fitted using Casa XPS software. The morphology of the particles was studied by FESEM (JSM 7800F), TEM, and High-Resolution Transmission Microscopy (HRTEM) in a Talos F200i. Fast Fourier Transforms (FFT) of high-resolution images were indexed with the help of CrystBox software.

The X-ray diffraction (XRD) patterns were recorded in a Bruker D8 Discover A25 instrument, with Cu Kα radiation. For the vibrational spectroscopy study, a Raman Jasco NRS-5500 instrument (532 nm) was employed.
Porosity and surface area were characterized by a Micromeritics instrument. After degassing, isotherms of nitrogen adsorption/desorption were measured at 77 K and carbon dioxide adsorption at 273 K.

Electrochemical characterization

The electrochemical behaviour was studied in sodium half-cells. The negative electrode was a piece of sodium. The positive electrode was a mixture of carbon (active material, 80%), carbon black (10%), and PVDF (10%) on aluminium disk as the current collector. As electrolyte solution, 1 M $NaClO_4$ in PC with 2% FEC was employed. The electrochemical experiments, galvanostatic cycling, galvanostatic intermittent titration (GITT), cyclic voltammetry (CV), and electrochemical impedance spectra (EIS), were conducted in a VMP instrument. The impedance spectra were recorded in three-electrode cells with a piece of Na as a counter electrode and another piece of Na as a reference electrode, within a frequency range between 500 kHz and 1 mHz.

Acknowledgments

The authors are grateful for the funding of the project PLEC2021-007779 entitled “Electrolytes and innovative electrodes for a new generation of sodium batteries for stationary applications (NABASTAT)”, financed by MCIN/AEI/10.13039/501100011033 and by the European Union “NextGenerationEU” /PRTR, and the *Junta de Andalucía* (group FQM288). They also acknowledge IQUEMA and SCAI (UCO) for the use of several experimental techniques.

Keywords: sodium-ion batteries • carbon • olive stones • synthesis

[1] a) D. A. Stevens, J. R. Dhan, *J. Electrochem. Soc.* **2001**, 148, A803; b) R. Alcántara, J. M. Jiménez-Mateos, J. L. Tirado, *J. Electrochem. Soc.* **2002**, 149, A201; c) R. Alcántara, G. F. Ortiz, P. Lavela, J. L. Tirado, R. Stoyanova, E. Zhecheva, *Chem. Mater.* **2006**, 18, 2293; d) R. Zhao, N. Sun, B. Xu, *Small Struct.* **2021**, 2, 2100132.

[2] a) J. Zhu, J. Roscow, S. Chandrasekaran, L. Deng, P. Zhang, T. He, K. Wang, L. Huang, *ChemSusChem* **2020**, 13, 1275; b) H. Moon, A. Innocenti, H. Liu, H. Zhang, M. Weil, M. Zarrabeitia, S. Passerini, *ChemSusChem* **2023**, 16, e202201713; c) A. Medina, R. Alcántara, J.L. Tirado, *J. Energy Storage* **2023**, 72, 108768; d) M. Kalibek, L. Rakhymbay, Z. Zhakiyeva, Z. Bakenov, S.-T. Myung, A. Konarov, *Carbon Resourc. Convers.* **2024**, 7, 100225; e) Z. Zhu, Y. Men, W. Zhang, W. Yang, F. Wang, Y. Zhang, Y. Zhang, X. Zeng, J. Xiao, C. Tang, X. Li, Y. Zhang, *eScience* preprint **2024**, 100249, https://doi.org/10.1016/j.esci.2024.100249.

[3] A. Gomez-Martin, J. Martinez-Fernandez, M. Ruttert, M. Winter, T. Placke, J. Ramirez-Rico, *Chem. Mater.* **2019**, 31, 7288; b) L. Rakhymbay, N. Bazybek, K. Kudaibergenov, S.-T. Myung, Z. Bakenov, A. Konarov, *J. Power Sources* **2024**, 602, 234347.

[4] N. Nieto, O. Noya, A. Iturrondobeitia, P. Sanchez-Fontecoba, U. Pérez-López, V. Palomares, A. Lopez-Urionabarrenechea, T. Rojo, *Batteries* **2022**, 8, 28.

[5] C. Agarwal, A.K. Pandey, *Environ. Sci.: Adv.* **2023**, 2, 1306.

[6] a) Y. Aniskevich, J. Ho Yu, J.-Y. Kim, S. Komaba, S.-T. Myung, *Adv. Energy Mater.* **2024**, 2304300; b) C. Bommier, X. Ji, P. A. Greaney, *Chem. Mater.* **2019**, 31, 658; c) Z. Hou, M. Jiang, D. Lei, X. Zhang, Y. Gao, J.-G. Wang, *Nano Res. preprint* **2024**, DOI: https://doi.org/10.1007/s12274-024-6448-1; d) L. Shi, W. Liu, F. Zhao, R. Liu, Y. Sun, C. Dong, G. Cheng, J. Ding, *J. Power Sources* **2024**, 596, 234093; e) B. Karaman, H. Tonnoir, D. Huo, B. Carré, A. F. Léonard, J. Castro Guiérrez, M.-L. Piedboeuf, A. Celzard, V. Fierro, C. Davaoisne, R. Janot, N. Job, *Carbon preprint* **2024**, DOI: https://doi.org/10.1016/j.carbon.2024.119077.

[8] C. Huang, J. Yin, W. Shi, Y. Cheng, X. Xu, *Mater. Today Energy* **2024**, 40, 101501.

[9] a) C. Chen, D. Yan, Y. V. Lim, L. Liu, X. Li, J. Chen, T. C. Li, Y. Zhu, J. Cai, Y. Huang, Y. Zhang, H. Y. Yang, *Carbon Energy* preprint **2024,** DOI: 10.1002/cey2.482; b) J. He, J. Du, C. Feng, Z. Xu, T. Li, H. Jia, C. Sun, K. Song, *Carbon* **2024**, 219,118825; c) G. Wang, W. Wang, X. He, J. Li, L. Yu, B. Peng, R. Liu, S. Zeng, G. Zhang, *Small* **2022**, 18, 2203288; d) J. Li, L. Yu, W. Wang, X. He, G. Wang, R. Liu, X. Ma, G. Zhang, *J. Mater. Chem. A* **2022**, 10, 9355.

[11] a) G. Rasines, P. Lavela, C, Macías, M. C. Zafra, J.L. Tirado, J. B. Parra, C. O. Ania, *Carbon* **2015**, 83, 262; b) R. Blume, D. Rosenthal, J.-P. Tessonnier, H. Li, A. Knop-Gericke, R. Schlögl, *ChemCatChem* **2015**, 7, 2871.

[12] a) A. Sadezky, H. Muckenhuber, H. Grothe, R. Niessner, U. Pöschl, *Carbon* **2005**, 43, 1731; b) A.C. Ferrari, J. Robertson, *Phys. Rev. B* **2000**, 61, 14095.

[13] a) J. Garrido, A. Linares-Solano, J.M. Martin-Martinez, M. Molina-Sabio, F. Rodriguez-Reinoso, R. Torregrosa, *Langmuir* **1987**, 3, 76; b) J. Serafin, J. Sreńscek-Nazzal, A. Kamińska, O. Paszkiewicz, B. Michalkiewicz, J. *CO_2 Util.* **2022**, 59, 101970; c) M. Maleki, H. Karimian, M. Shokouhimehr, R. Ahmadi, A. Valanezhad, A. Beitollahi, *Chem. Eng. J.* **2019**, 362, 469; d) C. Qiu, A. Li, D. Qiu, Y. Wu, Z. Jiang, J. Zhang, J. Xiao, R. Yuan, Z. Jiang, X. Liu, X. Chen, H. Song, *ACS Nano* preprint **2024**, DOI: 10.1021/acsnano.4c02046.

10.1002/cssc.202400708

[14] L. Bottoni, H. Darjazi, L. Sbrascini, A. Staffolani, S. Gabrielli, G. Pastore, A. Tombesi, F. Nobili, *ChemElectroChem* **2023**, 10, e202201117.

10.1002/cssc.202400708

WILEY VCH

RESEARCH ARTICLE

Entry for the Table of Contents

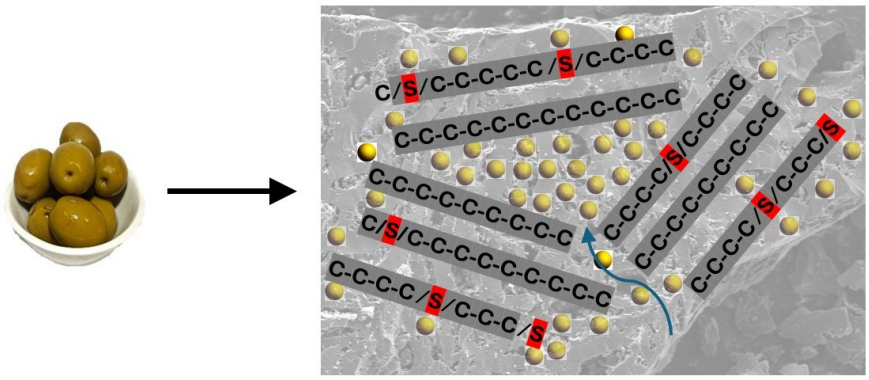

Worldwide production of olives for food and oil is very large, and a vast amount of waste in the form of olive stones is generated. Carbon for sodium-ion battery is obtained here from the stones of pickled olives. The method used provides that the carbon has optimized microstructure and porosity and sulfur atoms linked to carbon, resulting in superior electrochemical behavior.